GONG'94: Helio- and Astero-Seismology
ASP Conference Series, Vol. 76, 1995
R.K. Ulrich, E.J. Rhodes, Jr. and W. Däppen (eds.)

MICHELSON DOPPLER IMAGER (MDI) PERFORMANCE CHARACTERISTICS

I. ZAYER, M. MORRISON, T. POPE, W. ROSENBERG, T. TARBELL, A. TITLE, J. WOLFSON
Lockheed Palo Alto Research Laboratory (LPARL), 91-30/252,
3251 Hanover St., Palo Alto, CA 94304

R.S. BOGART, J.T. HOEKSEMA, P. MILFORD, P.H. SCHERRER, J. SCHOU
Center for Space Science & Astrophysics, ERL 328,
Stanford, CA 94305-4055

ABSTRACT An extensive calibration program of the Michelson Doppler Imager (MDI) instrument was carried out at LPARL prior to its delivery in April 1994. The instrument itself and the science objectives of the Solar Oscillations Investigation (SOI) are described in the preceding status report (Scherrer et al. 1994). The calibration program included performance measurements for each of MDI's subsystems (e.g., filter characteristics), as well as end-to-end tests of the flight instrument (derivation of an l-ν diagram from a time series of Dopplergrams). We present a brief description of the calibrations and a limited number of results.

INTRODUCTION

The calibrations were performed over a wide range of environmental conditions (including vacuum with the CCD cold) and with different light sources. Input light for the tests most often came from a stimulus telescope whose optical layout is almost identical to MDI's except for the absence of spectral filters. The beam can be deflected with a fast steering mirror to introduce known amounts of jitter into the instrument. A continuum lamp or a tunable laser can be used as a light source, and targets can be introduced at the stimulus focus. For solar observations, LPARL's heliostat provides an un-vignetted solar image.

The tests revealed a small number of effects that required a solution or additional characterization: an "ice-like" build-up on the cooled CCD camera, a large-scale intensity gradient caused by polarized beam-splitter coatings, wavelength non-uniformities in the Michelson interferometer, and a quantum-efficiency hysteresis (QEH) in the CCD. While these characteristics necessitate more elaborate calibration procedures than originally expected, MDI's performance will not compromise the proposed science objectives. The calibration program also provided valuable incentive for, and experience with, developing flight operations software and data analysis tools.

SPECTRAL PROPERTIES

The Lyot and Michelson filters were calibrated in the instrument using a tunable laser and sunlight as sources and the flight CCD camera as a detector. These measurements, summarized in Table I, are more accurate than measurements of the individual items made prior to assembly. M1 and M2 in Table I refer to the pair of Michelson interferometers.

TABLE I Filter Profile Parameters

Parameter	Measured Value	
MICHELSONS	M1	M2
Free Spectral Range	189 mÅ	377 mÅ
Tuning Contrast	99 %	99 %
Non-uniformity (laser)	60 mÅ p-p	160 mÅ p-p
Non-uniformity (sunlight)	20 mÅ p-p	50 mÅ p-p
Angular Sensitivity	± 22 mÅ	± 28 mÅ
Temperature Sensitivity	-9 mÅ/°C	-14 mÅ/°C
LYOT		
Central Wavelength	45 mÅ red of mean solar wavelength	
Profile Shape	465 mÅ FWHM; 7 & 2 % side-lobes @ ± 2.7 Å	
Uniformity	25 mÅ p-p	
Angular Sensitivity	0 - 65 mÅ	
Temperature Sensitivity	≤ 8 mÅ/°C	

Transmission Profile

The Michelsons were tuned for maximum transmission at multiple settings of the tunable laser wavelength while monitoring laser output intensity and wavelength. The main lobe is very well represented by a Gaussian. Near-simultaneous measurements of sunlight with MDI showed that the Ni I line was offset 45 mÅ to the red of the maximum transmission peak.

Wavelength Non-uniformity

Unfortunately, the tuning of the Michelson interferometers varies across their faces. Central wavelength maps have been made showing the spatial variation of the wavelength of peak transmission across each Michelson. The narrow line width of the tunable laser provides an ideal diagnostic tool; tuning maps were made with MDI in calibration mode (aperture imaged onto the focal plane) by filling the aperture with a collimated laser beam and taking a series of exposures while tuning each Michelson through its free spectral range. Analysis of the intensities yields the central wavelength at each position. This is done with 9 different pointings to map a large area of each Michelson and to measure the angular dependence of the central wavelength. The maps are made in a similar way using solar illumination, but the analysis determines the Michelson tuning at the solar line center. These maps look different from the laser maps due to different spatial and angular averaging involving both instrument geometry and solar effects (limb darkening, rotation, center-to-limb variation of the line

profile, etc.). Figure 1 shows solar Michelson maps of the type that will be made routinely during the mission. Detailed simulations are in progress to examine the correspondence of the laser and solar calibrations and to determine how to best use the solar maps for Doppler calibrations during the flight. Thermal transient tests indicate that mechanical stress in the vacuum-spaced interferometer legs is responsible for at least some of the non-uniformity.

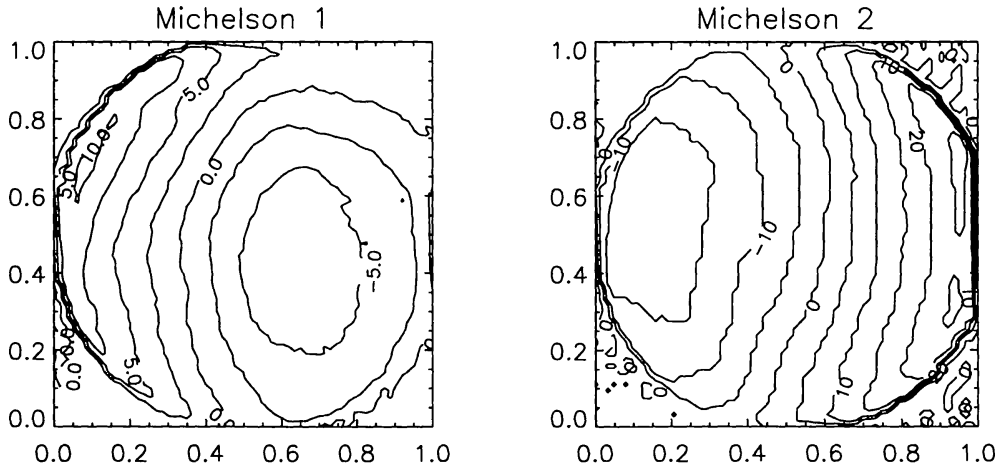

Fig. 1. Michelson central wavelength maps; solar calibration.

IMAGING PERFORMANCE

Focus

MDI's focus can be adjusted in orbit. The intent is to launch MDI in the center of its adjustable range so as to have maximum margin should the focus shift during lift-off. The telescope and detector are matched and focussed in the high resolution (HR) path. This would cause aliasing in the full disk (FD) path if it were co-focal due to under-sampling of the resolved spatial structures. A sufficient anti-aliasing measure was to simply build MDI with the FD path defocussed by two focus steps. Sharpness measurements using a grid target are routinely performed to verify the focus. Solar granulation will be used during the mission.

Resolution

To evaluate the image quality in both FD and HR paths, a resolution target is imaged in different positions within the field. The focus is stepped through a small range to guarantee exposures at best focus. The contrast in tri-bars of varying spatial frequency is evaluated to obtain the *square-wave* MTF in both the horizontal and vertical dimension. The resulting MTF's are plotted in the left panel of Figure 2 as dotted lines in comparison to the theoretical *sine-wave* MTF (solid line).

Distortion

The optical distortion has been measured in two different ways using a grid target: in one case, an MDI image is compared to theodolite measurements of the stimulus telescope output, and in the other case, changes in the shape of

grid elements are measured as a function of position within the field of view (FOV). The distortion in the nominal FD mode is a smooth radial compression increasing approximately as the square of the distance fron the center of the FOV with a value of $\leq$0.2% p-p. It is not expected to change with time and is thus irrelevant for Doppler observations, while for limb-figure observations it can be calibrated out. The magnetic signal is sensitive to the differential distortion between observations in the two circular polarizations, a map of which is presented in the right panel of Figure 2.

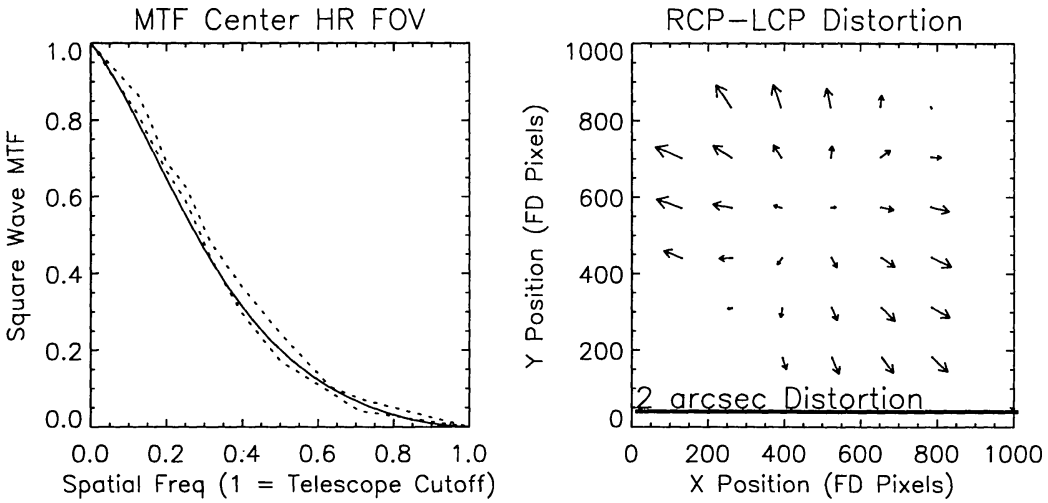

Fig. 2. Left panel: Square-wave MTF measured in x- and y- direction (dotted lines) and theoretical sine-wave MTF (solid line) at FOV center in HR; the spatial frequency unit is the telescope's cutoff frequency (0.86 arcsec^{-1}). Right panel: Relative distortion between exposures in LCP and RCP, the long horizontal bar represents one FD pixel (2 arcsec).

CCD Camera System

The primary routine test of the CCD performance is the measurement of a light transfer curve (LTC) in which the full well (FW), read noise, dark current, system gain, relative charge transfer efficiency (CTE) and linearity are determined. The LTC consists of a series of flat-field image pairs with increasing exposure times. Low-signal absolute CTE calibration was obtained earlier from Fe55 measurements by injecting known amounts of charge (5.9 keV X-rays) into the device. Figure 3 is a plot of the camera system's linearity residuals at -70°C calculated from sub-areas of 16x16 pixels within the central 256^2 portion of the CCD. The following values summarize the flight camera's performance at -70°C: maximum signal: >450 ke$^-$; read noise: 50 e$^-$; dark current: 0.3 e$^-$/s; system gain: 110 e$^-$/DN; CTE: >0.999995 (1/2 FW), >0.99998 (Fe55). Extensive proton damage tests have been carried out with LPARL's Van de Graaff accelerator and the expected end-of-mission CTE degradation was modelled (Zayer et al. 1993). The results together with the mission being near solar activity minimum indicate that the CTE should stay above the value of 0.9999 (acceptable MTF degradation).

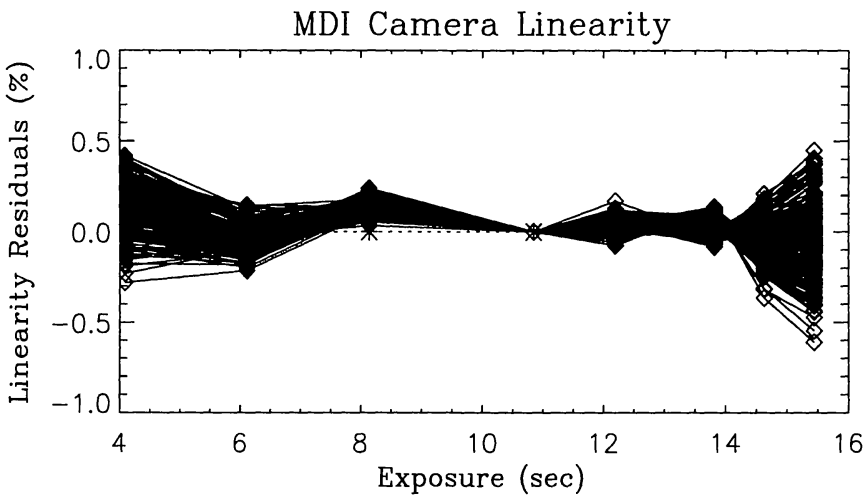

Fig. 3. Linearity residuals of the flight camera system; each line represents a 16x16pix sub-area within the central 256x256 portion of the CCD at -70°C.

Image Motion

HR images were used to investigate undesired image displacement due to rotation of optical elements (wedge). The location of the target grid is determined while the three relevant mechanisms (Michelson tuning motors and the polarization wheel) are rotated. The systematic image positions as a function of optical element orientation are contained within ±0.05 HR pixels (0.03 arcsec) for all motors.

Image Stabilization System (ISS)

The ISS has two main functions: a) to keep the filtergrams in a Doppler set co-registered to better than 0.02 arcsec and thereby avoid noise in Doppler measurements, and b) to avoid blurring of HR images by keeping the rms jitter during a typical 100 msec exposure below 0.15 arcsec. The performance was tested by introducing known amounts of jitter at known frequencies into a grid target image. Jitter reduction was measured in two different ways: (1) by measuring blurring of images with the ISS loop open and closed, and (2) by examining the error signals with a spectrum analyzer. The measurements (using an empirical calibration of blurring as a function of jitter) follow the predicted curve of the servo response as a function of frequency very closely. Calculations using the uncertain, but hopefully pessimistic, pointing jitter models for MDI on the SOHO satellite provide confidence of satisfactory on-orbit ISS performance.

OBSERVABLES

The measurement of Dopplergrams - MDI's primary data product - under all observing conditions (all MDI modes, paths, and polarizations) constituted a major aspect of the calibration effort, including several runs of full-day solar observations. The results, including the final l-ν diagram from a time-series of Dopplergrams are described in the preceding paper (Scherrer et al. 1994). Unlike in space, the solar image in our laboratory rotates throughout the day. This rotation introduces errors that have been used to an advantage: it proved to

be a valuable tool to probe non-uniformities in the filters. The planned in-flight calibration will mimic this by occasionally rotating the spacecraft.

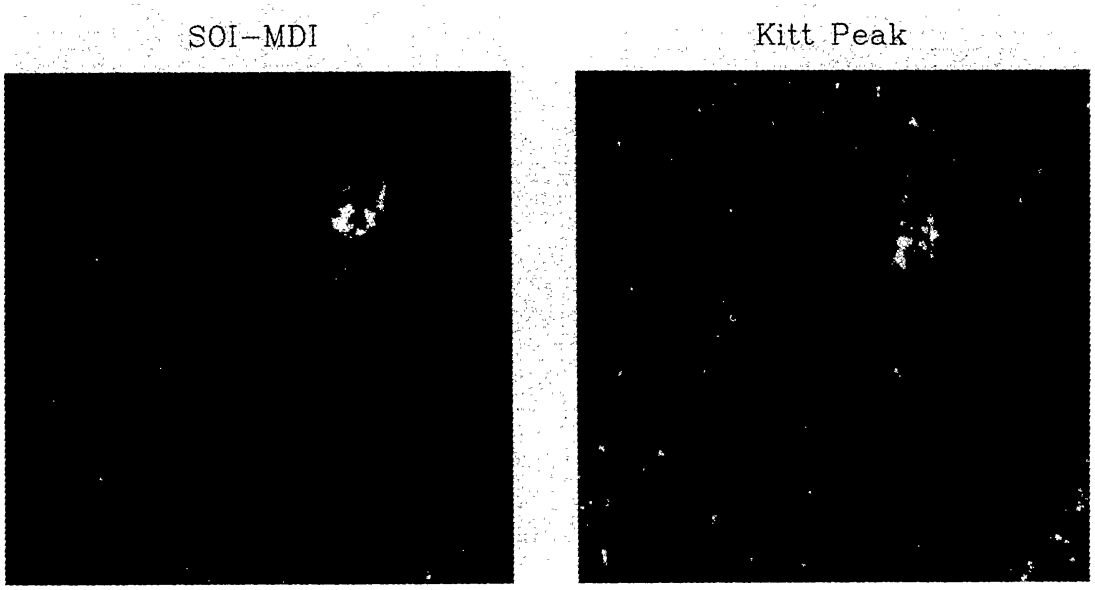

Fig. 4. Magnetograms obtained in MDI HR mode (left) and from Kitt Peak (right) on the same day (22. April 1994). The scales are not identical.

MDI observables also include continuum and line intensities, as well as magnetic field. The latter is computed as the difference of Dopplergrams taken in two orthogonal circular polarizations (RCP-LCP). Figure 4 shows a 40-second MDI HR magnetogram taken with the ISS engaged beside a KPVT magnetogram obtained a few hours earlier. Although the noise is somewhat higher in the ground-based MDI magnetogram, the signal distribution is very similar in the two images.

ACKNOWLEDGEMENTS

We wish to express our gratitude to the entire MDI team for their dedicated efforts to accomplish a task of this magnitude. We gratefully acknowledge NASA's sponsoring of this program under contract NAS5-30386, as well as the use of LPARL's solar and astrophysics laboratory facilities.

REFERENCES

Scherrer, P.H., R.S. Bogart, R. Bush, J.T. Hoeksema, P. Milford, J. Schou, W. Rosenberg, T. Tarbell, A. Title, J. Wolfson, I. Zayer 1994, in *GONG'94 Helio- and Astero-Seismology from Earth and Space*, eds. R.K. Ulrich, E.J. Rhodes, Jr. and W. Däppen, this volume.

Zayer, I., I. Chapman, D. Duncan, G. Kelly, K. Mitchell 1993, *Proc. SPIE* **1900**, p. 96.

PART VI
DATA ANALYSIS TECHNIQUES

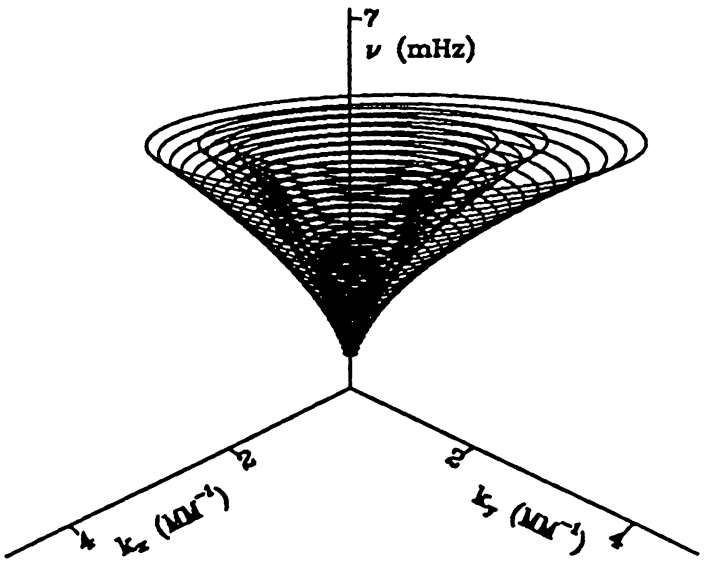

A theoretical picture of "trumpet" surfaces of high-degree oscillations. This model is a simulation of the trumpet surfaces obtained when a subraster is not tracked to remove surface rotation. See Hill, Figure 3.